Applied Radiation and Isotopes 180 (2022) 110055

Contents lists available at ScienceDirect

Applied Radiation and Isotopes

journal homepage: www.elsevier.com/locate/apradiso

Proton range monitoring based on picosecond detection using a Cherenkov radiation detector: A Monte Carlo study

Feng Tian [a], Changran Geng [a,b,c], Xiaobin Tang [a,b,c,*], Diyun Shu [a,c], Huangfeng Ye [a], Chunhui Gong [a,c]

[a] Department of Nuclear Science and Technology, Nanjing University of Aeronautics and Astronautics, 29 General Road, Jiangning District, Nanjing, 210016, China
[b] Key Laboratory of Nuclear Technology Application and Radiation Protection in Astronautic, Nanjing University of Aeronautics and Astronautics, Ministry of Industry and Information Technology, 29 General Road, Jiangning District, Nanjing, 210016, China
[c] Joint International Research Laboratory on Advanced Particle Therapy, Nanjing University of Aeronautics and Astronautics, 29 General Road, Jiangning District, Nanjing, 210016, China

ARTICLE INFO

Keywords:
Proton therapy
PbF_2 crystal
Cherenkov photons
Time of flight
Prompt gamma

ABSTRACT

In this study, we analyzed the performance of a PbF_2 crystal-based detector at proton range monitoring with Monte Carlo simulations. The correlations between the depth–dose and Cherenkov profiles showed that the changes in the peak position in the Cherenkov profiles corresponded to the changes in the corresponding depth–dose profiles. Moreover, the deviations between the changes in the peak positions in the two curves were generally less than 2 mm. The results also showed that the actual proton range could be obtained using flight time information. When the proton energy was 160 MeV, the peak position detected in the Cherenkov profile detected was 14.83 cm with a flight time of 5.3–5.4 ns (starting from the time when protons were emitted), and the actual proton range in polymethyl-methacrylate was 15 cm. Therefore, the accuracy of the proton range measurements could be improved and the absolute range obtained by using the fast and time-sensitive characteristics of the proposed Cherenkov radiator.

1. Introduction

The maximum proton dose will be deposited at the end of the range in a tissue, to form a sharp dose peak, i.e., the Bragg peak, and almost no dose deposition occurs after the Bragg peak (Daniel et al., 1998; Geng et al., 2016; Marafini et al., 2017). Due to the Bragg peak phenomenon, the dose in normal tissue distal to the tumor can be significantly reduced when proton therapy is used to treat tumors, thereby improving the therapeutic effect and reducing the risk of complications.

However, uncertainties when determining the incident proton range can have major impacts on the actually dose distribution applied due to the Bragg peak phenomenon (Knopf and Lomax, 2013). Deviations in the proton range are mainly caused by uncertainties when converting computed tomography images into proton stopping power maps (Paganetti and Harald, 2012), anatomical changes in different fractions under treatment, and other factors that make it difficult to assess with the necessary precision in clinical routines. A deviation in the Bragg peak location in patient will cause irreversible radiation damage to normal tissues near the boundary of the tumor. Therefore, real-time proton range verification is critical for ensuring the therapeutic effect.

Proton range verification has been widely studied through positron emission tomography (PET), and it has been applied in clinical studies at the GSI Helmholtzzentrum für Schwerionenforschung, Massachusetts General Hospital, and Heidelberg Ion Beam Therapy Center (Ario-Estrada et al., 2019; Moteabbed et al., 2011; Parodi, 2012; Zhu and Fakhri, 2013). However, this delayed gamma measurement method detects the coincident gamma rays from positron annihilation after/during treatment and it is severely affected by human washout. By contrast, prompt gamma (PG) detection is a promising alternative to real-time range verification, where it detects the characteristic gamma rays generated during proton travel (Krimmer et al., 2018; Min et al., 2006; Parodi and Polf, 2018). Most previous experiments in this field used detectors with collimators, such as planar or confocal multi-slit collimators, in order to reject photons that are not emitted from patients in the direction perpendicular to the beam axis. However, neutrons will interact with the collimator and produce a large amount of gamma radiation when they

* Corresponding author. Department of Nuclear Science and Technology, Nanjing University of Aeronautics and Astronautics, 29 General Road, Jiangning District, Nanjing, 210016, China.
E-mail address: tangxiaobin@nuaa.edu.cn (X. Tang).

https://doi.org/10.1016/j.apradiso.2021.110055
Received 10 December 2020; Received in revised form 25 November 2021; Accepted 29 November 2021
Available online 1 December 2021

travel through the collimator, and neutrons are scattered widely within the patient's body, and thus these gamma rays can adversely affect the proton range monitoring results (Biegun et al., 2012). Some studies have shown that there are specific time deviations between the generation of photons by neutrons in the collimator and the PG generated by primary protons (Biegun et al., 2012; Roellinghoff et al., 2014). Detectors with a fast time response may be able to effectively reduce the unfavorable effects of neutrons and improve the accuracy of range verification based on these time deviations by using the time-of-flight (TOF) method. Studies have demonstrated that the TOF method can obtain good range verification results (Dauvergne et al., 2020; Jacquet et al., 2021; Livingstone et al., 2021). However, most of these studies used scintillators as the detector materials and there is a significant light decay time when the scintillator is excited by incident gamma rays. This light decay time will have adverse effects on the time spectrum results and affect the accuracy. Therefore, using detectors with a short decay time can allow more accurate proton range verification based on the TOF method (Pausch et al., 2016).

The de-excitation process in lead fluoride (PbF_2) crystals is totally different compared with that in conventional scintillator materials. When penetrating a PbF_2 crystal, a photon deposits energy during its path of travel to generate secondary electrons. Polarization of the molecules occurs around the travel path when the speed of the electron in the PbF_2 crystal is faster than the speed of light in this type of material. The de-polarization process in these polarized molecules will produce Cherenkov photons with a specific direction of motion (Achenbach et al., 2012). These Cherenkov photons are generated almost instantaneously, i.e., no light decay time exists. Therefore, detectors based on PbF_2 crystals have an excellent time response capacity and they have been studied extensively in the field of TOF-PET (Alokhina et al., 2018; Korpar et al., 2011; Ota et al., 2018). The time resolution of detector based on PbF_2 crystal is better compared with that of detectors based on traditional scintillators. Therefore, compared with traditional scintillator detectors, using a detector based on PbF_2 crystals can more effectively exploit the time difference between different photons and it is expected to allow more accurate proton range monitoring. However, although the detectors based on PbF_2 crystals will have excellent time characteristics, the light yield of PbF_2 is lower than that of scintillators, which still limits the application of detectors based on PbF_2 crystals in some radiation detection fields. Some recent studies have investigated the TOF method based on PbF_2 crystals for proton range verification, but the performance of this method has not been comprehensively assessed (Jacquet et al., 2021).

In the present study, we developed a type of detector based on PbF_2 crystals instead of traditional scintillators to detect the time spectrum of PG with multi-plate collimators. The relationships were determined between the depth–dose profiles in phantom and Cherenkov profiles detected by an optical detector of mono-energetic protons. Finally, the feasibility of using this PbF_2 crystal-based detector for proton range detection was discussed in detail.

2. Material and methods

2.1. Software and physics lists

The Monte Carlo simulation software TOPAS 3.1.2 was used to study multiparticle transport in this study (Perl et al., 2012). TOPAS 3.1.2 is a particle therapy research-oriented Monte Carlo platform based on Geant4.10.3.p01. The physical model used in this study was based on "G4OpticalPhysics", "HadronPhysicsQGSP_BIC_HP", "G4DecayPhysics", "G4RadioactiveDecayPhysics", "G4HadronElasticPhysics", and "G4EMStandardPhysics_option3" (Allison et al., 2006; Asai, 2007).

2.2. Geometric setup and proton beam parameters

In this study, a polymethyl-methacrylate (PMMA; chemical composition of $C_5H_8O_2$ and density $\rho = 1.19$ g•cm $^{-3}$) phantom with dimensions of $20 \times 20 \times 50$ cm^3 was irradiated by a mono-energetic pencil beam with energy ranging from 145 to 200 MeV. The number of incident protons was 1×10^9, which is more than that used in a single beam spot in clinics. Studies have shown that for the same detector structure, the results obtained by simulating 1×10^8 protons are basically the same as those with 1×10^9 protons, and the counting error caused by statistical fluctuations will increase to a certain extent (Jacquet et al., 2021). Therefore, the simulation results obtained in the present study are of practical value. Further uncertainties caused by differences in the particle number and noise will be investigated in future studies. Irradiation of the surface of PMMA by the proton beam was 40 cm. The time when proton irradiation commenced was defined as the starting point when the TOF for proton emission was equal to zero. Collimators made of tungsten were placed on the side perpendicular to the incident direction, with a thickness of 2 mm, width of 40 cm, and length of 20 cm, and 101 collimators were placed over an interval of 2 mm. The collimators were placed 15 cm away from the surface of the phantom (Lin et al., 2016). The rear end of the collimator was connected to a block of PbF_2 crystal. The dimensions of the crystal were $36 \times 2 \times 40$ cm^3 and it was coupled to an optical detector to detect the collimated PG. The dimensions of the optical detector were $36 \times 0.2 \times 40$ cm^3 and it was made of silicon. The detection modules for the PbF_2 crystal and optical detector were wrapped with Teflon. The length of each sensitive area of optical detector along the Z axis was 2 mm and the center point of each sensitive area corresponded to the center point of the collimation hole. The optical detector was assumed to be a perfect detector, and thus only the Cherenkov light generated by the gamma rays from the corresponding collimation hole and that reached the sensitive area could be recorded. Given the time resolution of 100 ps achieved by PbF_2 crystal-based TOF-PETs, the time resolution in this study was assumed to be 100 ps (Korpar et al., 2015; Ota et al., 2018). The specific geometric structure is shown in Fig. 1.

2.3. Features and properties of PbF_2 crystals

The features and properties of PbF_2 crystals are shown in Table 1. The density of PbF_2 crystal is larger than that of Lutetium Oxyorthosilicate (LSO), Lutetium Yttrium Orthosilicate (LYSO) and Cerium Bromide ($CeBr_3$), which are commonly used in proton range monitoring with the TOF method. This high density indicates the superior capacity of PbF_2 crystals for absorbing photons.

The generation of Cherenkov photons requires a specific threshold energy and the minimum energy is the energy when the secondary electron velocity is equal to the velocity of the light in the PbF_2 crystal. The threshold energy for Cherenkov photons is related to the refractive index of the material, and the functional relationship is shown in Equation (1):

$$E_{min} = m_e c^2 \left(\frac{1}{\sqrt{1 - \frac{1}{n^2}}} - 1 \right) \quad (1)$$

where E_{min} is the threshold energy needed to generate Cherenkov photons in the PbF_2 crystal, $m_e c^2$ is the remaining energy of electrons in PbF_2, and n is the refractive index of PbF_2. The wavelength of Cherenkov photons ranges from ultraviolet to visible light (Fienberg et al., 2015). Thus, the threshold energy changes with the wavelength, and the specific results are shown in Fig. 2. The electron energy required to generate Cherenkov photons in PbF_2 crystals generally exceeds 0.1 MeV, which also indicates that the energy of the incident photons is greater than 0.1 MeV. Therefore, low-energy photons arriving at a Cherenkov radiator detector do not produce a signal output, thereby possibly reducing the adverse effects of scattered photons to some extent and further improving the accuracy of range monitoring. In order to simulate the

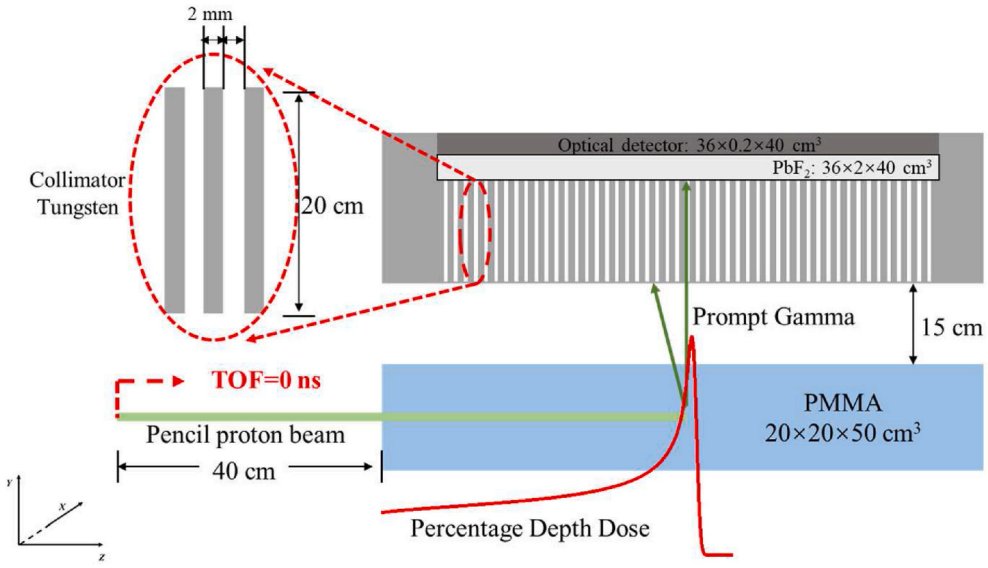

Fig. 1. Geometric structure used in this study.

Table 1
Features and properties of different crystals.

Properties	LSO/LYSO	$CeBr_3$	PbF_2
Decay Time (ns)	40	18	**None**
Density (g •cm^{-3})	7.2	5.2	**7.77**
Radiation Length (cm)	1.16	1.96	**0.93**
Emission Maximum (nm)	420	370	**200–800**

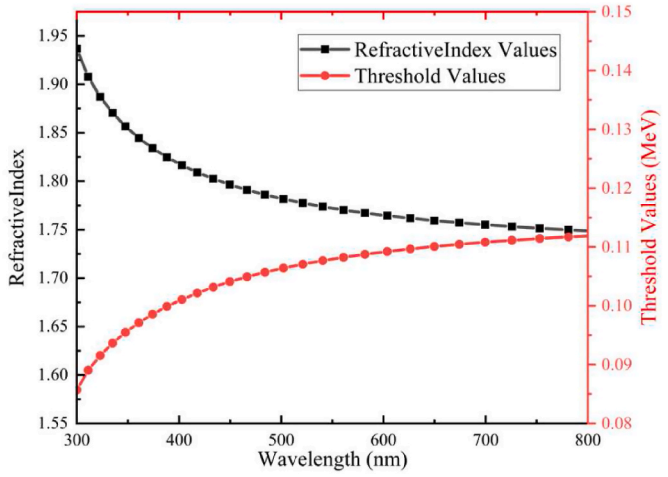

Fig. 2. Threshold energy for Cherenkov photons produced at different wavelengths.

generation and transportation of Cherenkov photon in the PbF_2 crystal, we set the refractive index, absorption length, and reflectivity of the PbF_2 crystal as corresponding to different photon wavelengths (Anderson et al., 1990; Malitson and Dodge, 1969).

3. Results and discussion

3.1. Correlations between depth–dose profiles in PMMA and Cherenkov profiles detected with mono-energetic protons

In this study, we analyzed the correlations between the changes in the depth–dose profiles in the PMMA phantom and the Cherenkov profiles generated in the PbF_2 crystal with different mono-energetic proton pencil beams.

Fig. 3 shows the Cherenkov distribution profiles obtained with different proton energies. The Cherenkov photons were generated by all particles that reached into the PbF_2 crystal after a proton point scan. For each energy, the peak position in the Cherenkov profile was significantly different from the peak position in the depth–dose curve. For the incident proton energies considered in this study, the deviations between the peak positions in the depth–dose curve and in the Cherenkov profiles in PbF_2 were about 6 cm. Thus, some particles reached into the PbF_2 crystal and degraded the accuracy of proton range verification. Therefore, the actual proton range could not be obtained based on the peak positions of the Cherenkov photons. However, the peak positions of Cherenkov photons changed as the energy of the incident proton changed. Therefore, we analyzed the correlations between the positional changes in the depth–dose curve and in the Cherenkov profiles. In particular, we focused on the changes in the peak position and the 80%

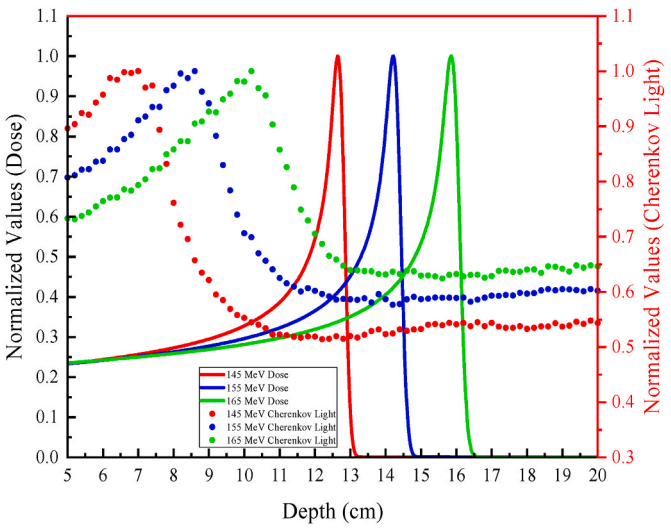

Fig. 3. Dose and Cherenkov light distribution for different incident protons with energies of 145, 155, and 165 MeV. The solid line in the figure represents the normalized depth–dose distribution in PMMA. The points in the figure represent the normalized distribution of Cherenkov light generated in the PbF_2 crystal along the direction of incident protons.

distal falloff position in the Cherenkov profiles and depth–dose curve under different energies.

The results are shown in Table 2. When the proton energy increased from 145 MeV to 155 MeV, the peak position in the depth–dose curve changed by 1.58 cm and the 80% distal falloff position changed by 1.58 cm. Accordingly, the peak position in the Cherenkov profiles detected by the optical detector changed by 1.62 cm and the 80% distal falloff position changed by 1.66 cm. The deviations between the changes in the depth–dose curve and Cherenkov profile were all less than 2 mm, thereby meeting the accuracy requirements for proton range monitoring. Similarly, when the proton energy increased from 145 MeV to 165 MeV, the peak position in the depth–dose curve changed by 3.2 cm and the 80% distal falloff position changed by 3.26 cm. Accordingly, the peak position in the Cherenkov profiles detected by the optical detector changed by 3.26 cm and the 80% distal falloff position changed by 3.49 cm. The deviations between the changes in the depth–dose curve and Cherenkov profile were generally less than 2 mm, expect for the deviation between the 80% distal falloff position in the depth–dose curve and Cherenkov profiles. These results indicate that the range changes caused by changes in the incident proton energy can be monitored using a detector based on PbF_2 crystal.

3.2. Correlations between the peak position in Cherenkov profile and actual proton range based on the TOF method with proton energies of 160 and 200 MeV

Thus, we evaluated the performance of PbF_2 crystal-based detectors at proton range verification to monitor the range changes. Next, we focused on the absolute proton range obtained based on the peak position in the Cherenkov profile with the TOF method.

We employed the TOF method to perform real-time monitoring of the proton range, and thus the time information for photons in different components was crucial. We recorded the PG distribution and neutron distribution crossing the PMMA surface at different flight times for PG rays with characteristic energies of 4.44 MeV, 5.25 MeV, and 6.13 MeV. Therefore, we analyzed the time information for gamma rays with energies from 4 MeV to 7 MeV. Fig. 4 shows the time information for particles with different proton energies. The flux of the PG rays recorded on the PMMA surface was in the same order of magnitude as the neutron flux. Under the geometry configuration shown in Fig. 1, the time required for PG rays to pass through the PMMA was around 4 ns and that for neutrons was 5–6 ns. This deviation indicates that the PG and neutrons were generated almost simultaneously. TOF information was then recorded for the photons generated by primary protons and neutrons that arrived at the surface of the PbF_2 crystal. The flux of the PG rays that reached the detector dropped significantly due to the collimating effect of the collimator. As expected, the neutrons interacted with the collimator during their passage to produce a considerable amount of gamma rays. Compared with the PG rays, the flux characteristics of these gamma rays were in the same order of magnitude as the PG rays. The gamma rays generated by neutrons mainly reached the detector about 3 ns later than the PG rays. Considering that the Cherenkov photons were generated almost instantaneously, the Cherenkov photons detected within 5–6 ns were used to analyze the relationship between the distribution of Cherenkov photons and the proton range.

Table 2
Characteristic positions in depth–dose curves and Cherenkov profiles with incident protons of different energies.

Energy (MeV)	Peak position in percentage depth–dose curve (PDD) (cm)	Peak position in Cherenkov profile (cm)	80% distal falloff in PDD (cm)	80% distal falloff in Cherenkov profile (cm)
145	12.64	≈6.76	12.78	≈7.89
155	14.22	≈8.38	14.36	≈9.55
165	15.84	≈10.02	16.01	≈11.38

According to the analysis described above, the time required for the PG produced by primary protons to reach the detector was about 5–6 ns. Thus, the Cherenkov profiles were obtained in three periods, i.e., TOF <5 ns, TOF <6 ns, and 5 ns < TOF <6 ns. The two-dimensional distributions of the Cherenkov photons detected by the perfect detector are shown in Fig. 5. At TOF <5 ns (i.e., by integrating the Cherenkov photons detected between 0 and 5 ns), the PG generated by the incident proton at the end of its range did not reach the Cherenkov radiator detector to generate a Cherenkov signal. According to the distribution of the Cherenkov photons at TOF <6 ns (i.e., by integrating the Cherenkov photons detected between 0 and 6 ns), the Cherenkov peak existed at a depth of 14–15 cm in the direction of proton motion. This finding indicates that the PG generated at the end of the proton range reached the Cherenkov radiator detector during the period from 5 to 6 ns. Subsequently, the distribution of the Cherenkov photons from 5 to 6 ns was analyzed at intervals of 0.1 ns (i.e., by integrating the Cherenkov photons detected within each 0.1 ns interval). The distribution results shown in Fig. 6 indicated that the distribution of the Cherenkov photons contained a distinct peak position, which gradually approached the position of the Bragg peak of the incident proton as the flight time increased. In the interval from 5.3 to 5.4 ns, the peak position in the Cherenkov profile was at about 14.83 cm, which is comparable to the proton range for 15 cm, with a deviation of 1.70 mm. No noticeable peak position was observed in the Cherenkov photon distribution in subsequent time intervals. Therefore, detection of the absolute position in the proton range in actual proton therapy can be achieved based on the fast time response of the PbF_2 crystal-based detector with a measurement error less than 2 mm. The Cherenkov profiles in Figs. 3 and 6 show that the shifts in the Cherenkov light distribution and proton range were clearly different, possibly due to the delayed gamma rays generated by neutron interactions and other sources, such as activated radioisotopes.

The flight times of protons in PMMA changed as the energy of the incident proton increased. As shown in Fig. 7, the TOF for PG rays that reached the PMMA surface changed as the energy of the incident protons changed. Thus, we analyzed the distribution of the Cherenkov photons generated during a flight time of 5–6 ns, as shown in Fig. 7(a), which indicates that the highest yield position of the Cherenkov photons exceeded 20 cm. The relationship between the distribution of Cherenkov photons that reached the surface of perfect detector in each period and the actual percentage depth–dose (PDD) curve of the protons was analyzed in the time interval from 0.1 ns, as shown in Fig. 7(b). As the flight time increased, the peak position of the Cherenkov photons gradually approached the true depth–dose curve peak position for the incident protons. In the period from 5.6 to 5.7 ns, the peak position in the Cherenkov profile was 22 cm and the proton range was 22.09 cm. Therefore, the PbF_2 crystal-based detector can be used for range monitoring during proton therapy when the energy of the incident protons changes.

3.3. Accuracy of TOF PG detection based on a Cherenkov radiator material when the proton range is changed by a medium with an uneven distribution

As described above, we used a PbF_2 crystal-based detector to perform TOF screening of picosecond-level PG to allow the real-time in vivo monitoring of the proton range with a homogeneous PMMA model. However, the actual proton range in the human body is often affected by the presence of air, bone, and other components of the complex human tissue structure. Therefore, we analyzed the performance of a Cherenkov radiator detector when the proton range is changed by a medium with an uneven distribution.

A layer of air with a thickness of 2 cm was set in the travel path and the incident proton energy was 160 MeV. The distribution of the Cherenkov photons obtained by the perfect detector within 6 ns is shown in Fig. 8(a). The position and structure of the air layer in the Cherenkov profile at TOF <6 ns, and the position distribution of the Cherenkov

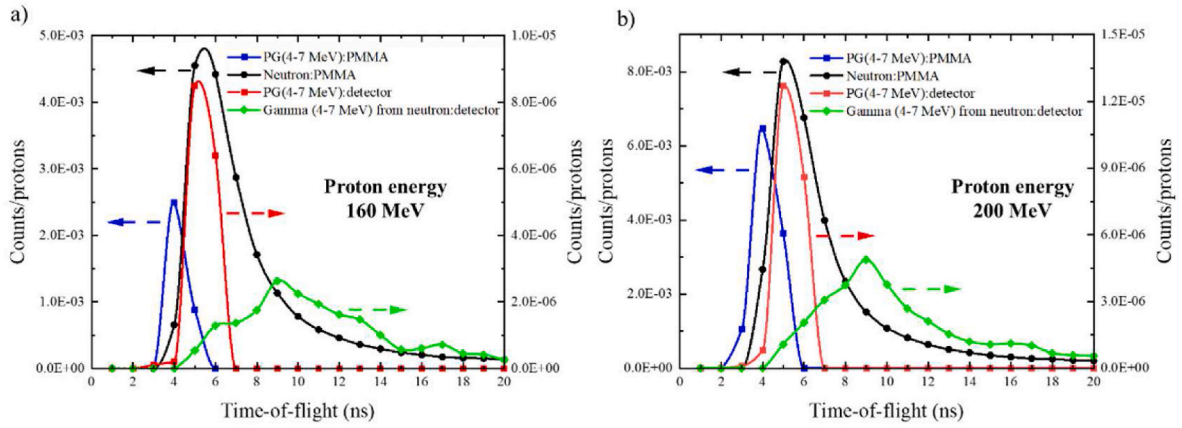

Fig. 4. Time information for PG rays, secondary neutrons, and gamma rays generated by neutrons with different proton energies. The blue and black curves indicate the time information for PG rays and neutrons that passed through the PMMA surface, respectively. The red and green curves indicate the time information for PG rays and gamma rays generated by neutrons that reached the surface of the PbF_2 crystal, respectively. (For interpretation of the references to colour in this figure legend, the reader is referred to the Web version of this article.)

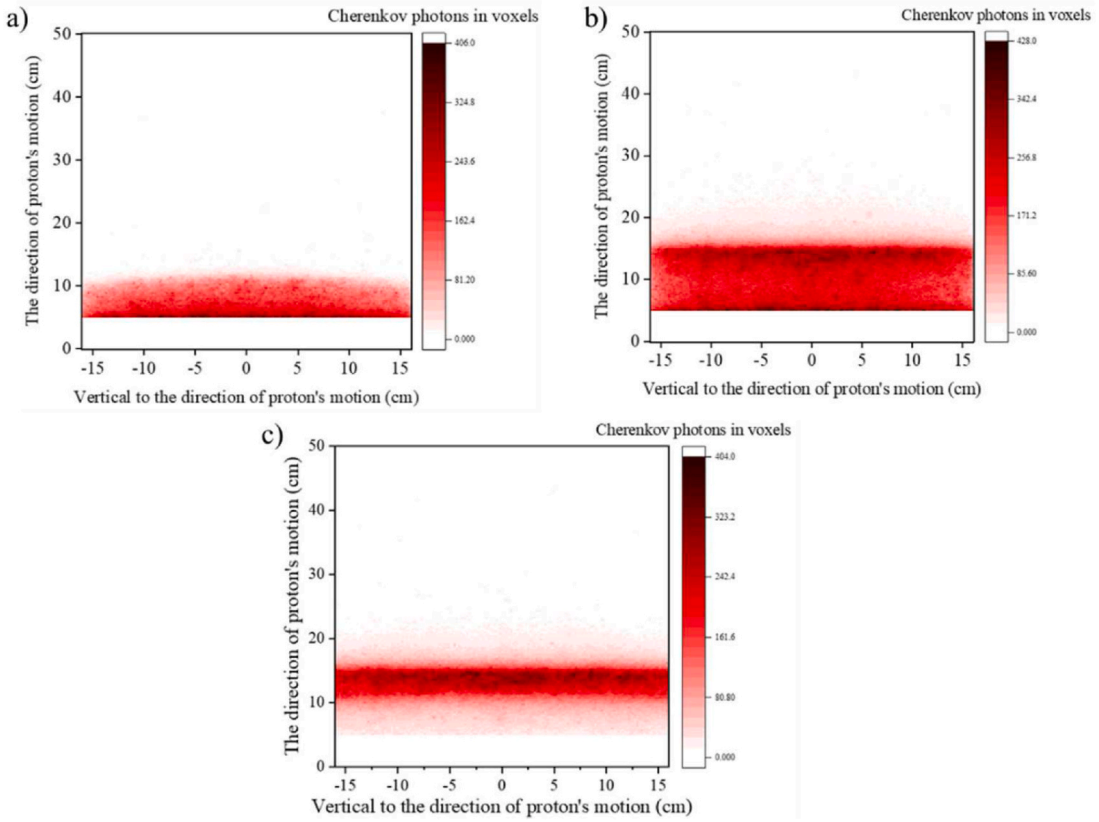

Fig. 5. Distributions of Cherenkov photons in different periods: (a) (left) Cherenkov distribution at TOF <5 ns; (b) (right) Cherenkov distribution at TOF <6 ns; (c) (bottom) Cherenkov distribution at 5 ns < TOF <6 ns.

photons generated in the PbF_2 crystal and detected by the perfect detector were analyzed at a time interval of 0.1 ns. The results indicated that this detector can potentially be applied in medical imaging. In each period, a distinct peak appeared in the generated Cherenkov photons and the position of this peak gradually approached the peak of the true PDD curve for the incident protons as the flight time increased. The peak of the Cherenkov photons matched perfectly with the peak position for the PDD in the period from 5.5 ns < TOF <5.6 ns. Thus, the Cherenkov detector based on PbF_2 crystal could accurately detect small changes in the proton range due to changes in the human tissue structure.

The light yield of the PbF_2 crystal is much lower than that of common scintillators but the maximum number of Cherenkov photons recorded in each detection region during a specific period was several hundred in these simulations. However, PG rays are only generated near the end of range due to the Bragg characteristic of the proton range. In addition, Cherenkov photons are generated in a specific region in the detector based on PbF_2 crystal at different TOFs. Thus, a proton range with different energies can be measured by using the Cherenkov radiator detector.

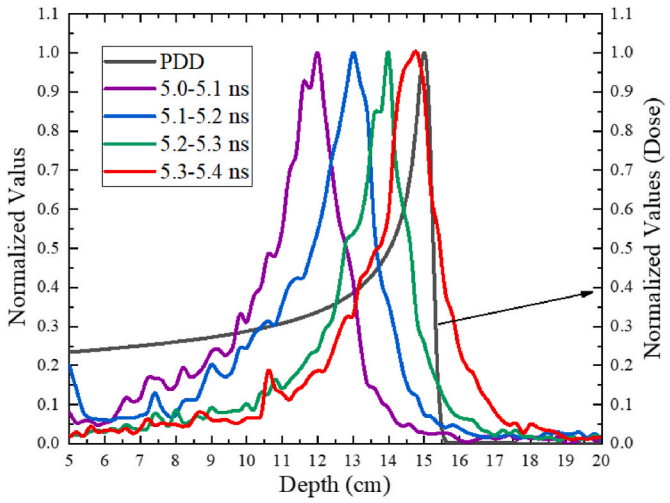

Fig. 6. Distribution of Cherenkov photons when 5 ns < TOF <6 ns at time intervals of 0.1 ns.

4. Conclusion

The application of the TOF method can help to improve the accuracy of proton range measurements. However, the traditional scintillator materials exhibit a certain light decay time, which may cause errors during proton range verification with PG detection. In this study, we proposed the replacement of traditional scintillator materials with PbF_2 crystal, which is a pure Cherenkov radiator that does not exhibit the light decay time phenomenon, and analyzed the performance of this detector at proton range monitoring. The measurement results showed that changes in the actual proton range could be determined by measuring the change in the peak position in the Cherenkov profile. Moreover, the deviation between the changes in the peak position in the two curves was generally less than 2 mm, which meets the clinical requirements. Absolute range monitoring based on the TOF method detected a noticeable peak in the Cherenkov profile generated in the PbF_2 crystal in the direction of proton motion at each time interval within 5–6 ns in accordance with the geometric structure employed in this study. As the flight time increased, the peak position gradually approached the end of the actual range of the proton. Moreover, at a certain time, the peak position in the Cherenkov profile matched perfectly with the position of the Bragg peak of the primary proton in PMMA. In addition, no significant peak was detected in the Cherenkov distribution after a certain time. Therefore, detection based on PbF_2 crystals can significantly improve the accuracy of proton range

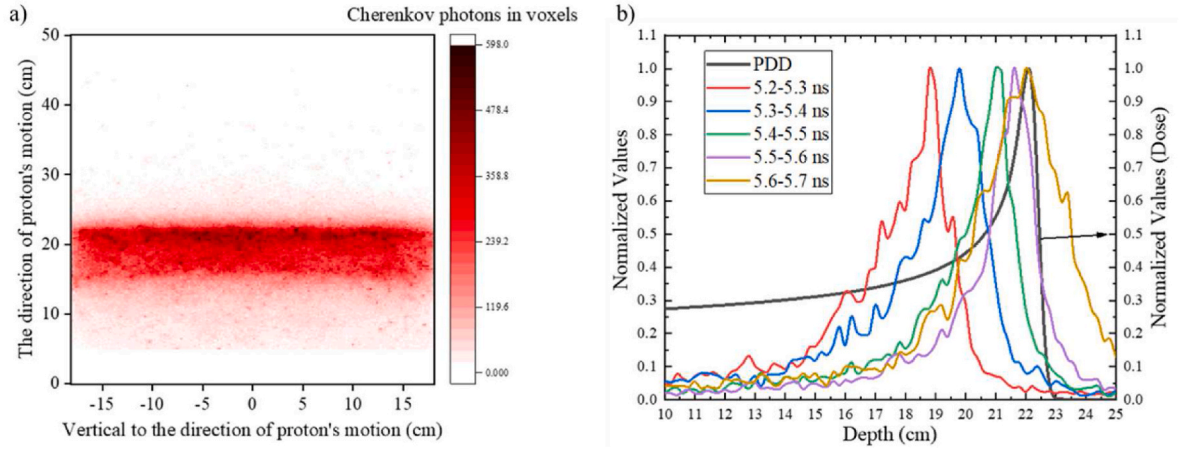

Fig. 7. Distribution of Cherenkov photons when the primary energy is 200 MeV: (a) (left) two-dimensional distribution of Cherenkov photons at 5 ns < TOF <6 ns; (b) (right) relationship between the peak position in the Cherenkov profile and the true PDD curve.

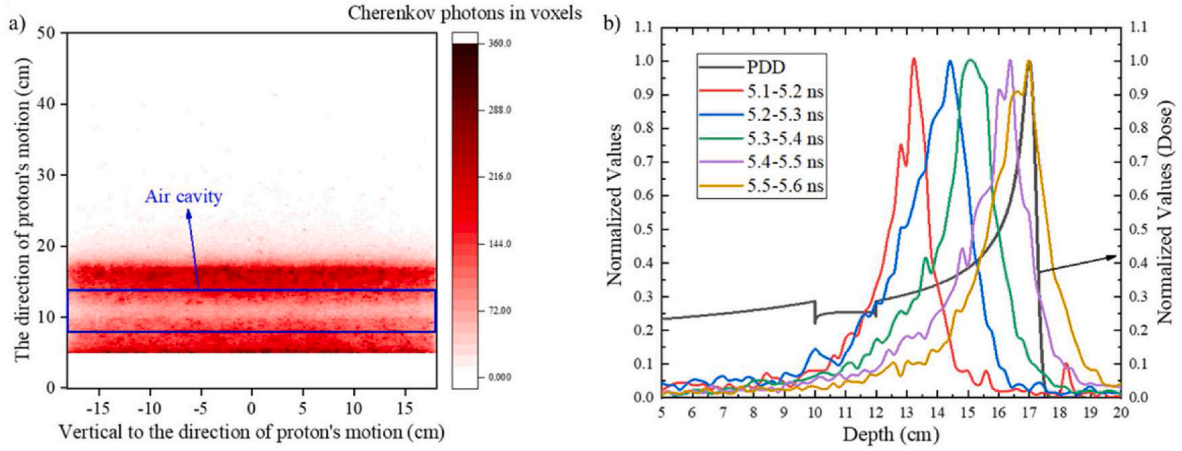

Fig. 8. Distribution of Cherenkov photons with a layer of air in the proton path: (a) (left) two-dimensional distribution of Cherenkov photons at TOF <6 ns; (b) (right) relationship between the Cherenkov profile and true PDD curve.

monitoring and the absolute proton range can be obtained with the TOF method. However, this study focused mainly on theoretical analysis of the proposed method. The number of simulated particles was more than the number of protons emitted in an actual spot scan. Therefore, the results obtained in this study have value as references for some fields such as high-dose therapy or flash therapy. However, in order to apply this method in low-dose therapy or experimental conditions in the future, it will be necessary to explore factors that influence the measurement accuracy, such as statistical errors caused by the number of protons, detector structure, and electronic noise.

Author statement

Feng Tian : Conceptualization, Methodology, Software, Validation, Formal analysis, Investigation, Data Curation, Writing–Original Draft, Writing–Review & Editing, Visualization. **Changran Geng** : Methodology, Writing–Original Draft, Writing–Review & Editing, Funding acquisition, Supervision. **Xiaobin Tang** : Writing–Original Draft, Writing–Review & Editing, Funding acquisition, Supervision, Project administration. **Diyun Shu** : Formal analysis, Writing–Original Draft, Writing–Review & Editing, Funding acquisition. **Huangfeng Ye** : Investigation, Writing–Original Draft, Writing–Review & Editing. **Chunhui Gong** : Writing–Original Draft, Writing–Review & Editing, Funding acquisition.

Declaration of competing interest

The authors declare that they have no known competing financial interests or personal relationships that could have appeared to influence the work reported in this paper.

Acknowledgments

This study was supported by the National Natural Science Foundation of China [Grant Nos. 11905106, and 12005102], the Natural Science Foundation of Jiangsu Province [Grant No.BK20190410], and the China Postdoctoral Science Foundation [Grant No.2019M651829].

References

Achenbach, P., Baunack, S., Grimm, K., Hammel, T., Harrach, D.V., Ginja, A.L., Maas, F. E., Schilling, E., Ströher, H., 2012. Measurements and simulations of Cherenkov light in lead fluoride crystals. Nucl. Instrum. Methods Phys. Res. A 465, 318–328.

Allison, J., Amako, K., Apostolakis, J., Araujo, H., Dubois, P.A., Asai, M., Barrand, G., Capra, R., Chauvie, S., Chytracek, R., 2006. Geant4 developments and applications. IEEE Trans. Nucl. Sci. 53, 270–278.

Alokhina, M., Canot, C., Bezshyyko, O., Kadenko, I., Tauzin, G., Yvon, D., Sharyy, V., 2018. Simulation and optimization of the Cherenkov TOF whole-body PET scanner. Nucl. Instrum. Methods Phys. Res. 912, 378–381.

Anderson, D., Kobayashi, M., Woody, C., Yoshimura, Y., 1990. Lead fluoride: an ultra-compact Cherenkov radiator for EM calorimetry. Nucl. Instrum. Methods Phys. Res. Sect. A Accel. Spectrom. Detect. Assoc. Equip. 290, 385–389.

Ario-Estrada, G., Mitchell, G.S., Kim, H., Du, J., Cherry, S.R., 2019. First Cerenkov charge-induction (CCI) TlBr detector for TOF-PET and proton range verification. Phys. Med. Biol. 64, 175001.

Asai, M., 2007. Geant4-A simulation toolkit. Nucl. Instrum. Methods Phys. Res. 506, 250–303.

Biegun, A.K., Seravalli, E., Lopes, P.C., Rinaldi, I., Pinto, M., Oxley, D.C., Dendooven, P., Verhaegen, F., Parodi, K., Crespo, P., 2012. Time-of-flight neutron rejection to improve prompt gamma imaging for proton range verification: a simulation study. Phys. Med. Biol. 57, 6429.

Daniel, W., Miller, 1998. A review of proton beam radiation therapy. Med. Phys. 22, 1943.

Dauvergne, D., Allegrini, O., Caplan, C., Chen, X., Zoccarato, Y., 2020. On the role of single particle irradiation and fast timing for efficient online-control in particle therapy. Front. Phys. 8, 567215.

Fienberg, A.T., Alonzi, L.P., Anastasi, A., Bjorkquist, R., Cauz, D., Fatemi, R., Ferrari, C., Fioretti, A., Fankenthal, A., Gabbanini, C., 2015. Studies of an array of PbF2 Cherenkov crystals with large-area SiPM readout. Nucl. Instrum. Methods Phys. Res. Sect. A Accel. Spectrom. Detect. Assoc. Equip. 783, 12–21.

Geng, C., Moteabbed, M., Seco, J., Gao, Y., Paganetti, H., 2016. Dose assessment for the fetus considering scattered and secondary radiation from photon and proton therapy when treating a brain tumor of the mother. Phys. Med. Biol. 61, 683.

Jacquet, M., Marcatili, S., Gallin-Martel, M.L., Bouly, J.L., Testa, E., 2021. A time-of-flight-based reconstruction for real-time prompt-gamma imaging in proton therapy. Phys. Med. Biol. 66, 135003.

Knopf, A.C., Lomax, A., 2013. In vivo proton range verification: a review. Phys. Med. Biol. 58, 131–160.

Korpar, S., Krizan, P., Dolenec, Pestotnik, R., 2015. Cherenkov TOF PET with silicon photomultipliers. Nucl. Instrum. Methods Phys. Res. Sect. A Accel. Spectrom. Detect. Assoc. Equip. 804, 127–131.

Korpar, S., Dolenec, R., Krizan, P., Pestotnik, R., Stanovnik, A., 2011. Study of TOF PET using Cherenkov light. Nucl. Instrum. Methods Phys. Res. 654, 532–538.

Krimmer, J., Dauvergne, D., Létang, J., Testa, É., 2018. Prompt-gamma monitoring in hadrontherapy: a review. Nucl. Instrum. Methods Phys. Res. Sect. A Accel. Spectrom. Detect. Assoc. Equip. 878, 58–73.

Lin, H.H., Chang, H.T., Chao, T.C., Chuang, K.S., 2016. A comparison of two prompt gamma imaging techniques with collimator-based cameras for range verification in proton therapy. Radiat. Phys. Chem. 137, 144–150.

Livingstone, J., Dauvergne, D., Etxebeste, A., Fontana, M., Gallin-Martel, M.-L., Huisman, B., Létang, J.M., Marcatili, S., Sarrut, D., Testa, E., 2021. Influence of sub-nanosecond time of flight resolution for online range verification in proton therapy using the line-cone reconstruction in Compton imaging. Phys. Med. Biol. 66, 125012.

Malitson, I., Dodge, M., 1969. Refraction and dispersion of lead fluoride. J. Opt. Soc. Am. 500. AMER INST PHYSICS CIRCULATION FULFILLMENT DIV, 500 SUNNYSIDE BLVD, WOODBURY ….

Marafini, Paramatti, Pinci, Battistoni, Collamati, 2017. Secondary radiation measurements for particle therapy applications: nuclear fragmentation produced by 4He ion beams in a PMMA target. Phys. Med. Biol. 62, 1291.

Min, C.-H., Kim, C.H., Youn, M.-Y., Kim, J.-W., 2006. Prompt gamma measurements for locating the dose falloff region in the proton therapy. Appl. Phys. Lett. 89, 183517.

Moteabbed, M., España, S., Paganetti, H., 2011. Monte Carlo patient study on the comparison of prompt gamma and PET imaging for range verification in proton therapy. Phys. Med. Biol. 56, 1063–1082.

Ota, R., Yamada, R., Moriya, T., Hasegawa, T., 2018. Cherenkov radiation-based three-dimensional position-sensitive PET detector: a Monte Carlo study. Med. Phys. 45, 1999–2008.

Paganetti, Harald, 2012. Range uncertainties in proton therapy and the role of Monte Carlo simulations. Phys. Med. Biol. 57, 99–117.

Parodi, K., 2012. PET monitoring of hadrontherapy. Nucl. Med. Rev. Cent. E Eur. 15, 37–42.

Parodi, K., Polf, J.C., 2018. In vivo range verification in particle therapy. Med. Phys. 45, e1036–e1050.

Pausch, G., Petzoldt, J., Berthel, M., Enghardt, W., Fiedler, F., Golnik, C., Hueso-González, F., Lentering, R., Rmer, K., Ruhnau, K., 2016. Scintillator-based high-throughput fast timing spectroscopy for real-time range verification in particle therapy. IEEE Trans. Nucl. Sci. 63, 664–672.

Perl, J., Shin, J., Schümann, J., Faddegon, B., Paganetti, H., 2012. TOPAS: an innovative proton Monte Carlo platform for research and clinical applications. Med. Phys. 39, 6818–6837.

Roellinghoff, F., Benilov, A., Dauvergne, D., Dedes, G., Freud, N., Janssens, G., Krimmer, J., Létang, J., Pinto, M., Prieels, D., 2014. Real-time proton beam range monitoring by means of prompt-gamma detection with a collimated camera. Phys. Med. Biol. 102, 1327–1338.

Zhu, X., Fakhri, G.E., 2013. Proton therapy verification with PET imaging. Theranostics 3, 731–740.